PROCEEDINGS A

royalsocietypublishing.org/journal/rspa

Research

Cite this article: Geng L, Zhang W, Zhang X, Zhou X. 2021 Chiral mode transfer of symmetry-broken states in anti-parity-time-symmetric mechanical system. *Proc. R. Soc. A* **477**: 20210641.
https://doi.org/10.1098/rspa.2021.0641

Received: 6 August 2021
Accepted: 12 November 2021

Subject Areas:
mechanical engineering, solid-state physics, structural engineering

Keywords:
non-Hermitian mechanical system, anti-parity-time symmetry, exceptional point, time-modulated medium, chiral mode transfer

Author for correspondence:
Xiaoming Zhou
e-mail: zhxming@bit.edu.cn

Chiral mode transfer of symmetry-broken states in anti-parity-time-symmetric mechanical system

Linlin Geng[1], Weixuan Zhang[2], Xiangdong Zhang[2] and Xiaoming Zhou[1]

[1]Key Laboratory of Dynamics and Control of Flight Vehicle of Ministry of Education, School of Aerospace Engineering, and [2]Key Laboratory of Advanced Optoelectronic Quantum Architecture and Measurements of Ministry of Education, School of Physics, Beijing Institute of Technology, Beijing 100081, People's Republic of China

WZ, 0000-0002-7725-8814; XMZ, 0000-0002-3240-9789

Non-Hermitian systems with parity-time (PT) symmetry reveal rich physics beyond the Hermitian regime. As the counterpart of conventional PT symmetry, anti-parity-time (APT) symmetry may lead to new insights and applications. Complementary to PT-symmetric systems, non-reciprocal and chiral mode switching for symmetry-broken modes have been reported in optics with an exceptional point dynamically encircled in the parameter space of an APT-symmetric system. However, it has remained an open question whether and how the APT-symmetry-induced chiral mode transfer could be realized in mechanical systems. This paper investigates the implementation of APT symmetry in a three-element mass–spring system. The dynamic encircling of an APT-symmetric exceptional point has been implemented using dynamic-modulation mechanisms with time-driven stiffness. It is found that the dynamic encircling of an exceptional point in an APT-symmetric system with the starting point near the symmetry-broken phase leads to chiral mode switching. These findings may provide new opportunities for unprecedented wave manipulation in mechanical systems.

Electronic supplementary material is available online at https://doi.org/10.6084/m9.figshare.c.5754125.

THE ROYAL SOCIETY PUBLISHING

1. Introduction

Non-Hermitian quantum-mechanics systems protected by parity-time (PT) symmetry have attracted considerable attention in recent years [1–3]. A purely real energy spectrum can still be observed in these systems, and there exists a symmetry-breaking threshold point, called the exceptional point (EP), at which eigenvalues and eigenvectors coalesce simultaneously [4,5]. A variety of intriguing properties have been found at EPs [6–10], which provide new schemes for controlling waves using balanced gain and loss. Based on the linkage between non-Hermitian quantum-mechanical and classical wave systems, the EP phenomenon associated with PT symmetry has been rapidly extended to acoustic [11–13] and elastodynamic realms [14–17]. Anomalous wave transport properties induced by EPs, such as asymmetric wave scattering [14,18,19], unidirectional sound focusing [13] and enhanced sensitivity [16,17], have been revealed. Another topic of particular interest relates to the eigenvalue topological structure and unique mode-switching manipulation around an EP. It has been revealed that adiabatically encircling an EP of degeneracy would result in an eigenstate exchange owing to the unique topological structure [20–22]. This phenomenon has been demonstrated experimentally in microwave [22] and acoustic [23] cavities by independently measuring the spectra and eigenfields at different locations on a parametric loop enclosing an EP. On the other hand, when considering a dynamic encircling, non-adiabatic transitions (NATs) [24] occur, leading to a robust chiral behaviour [25] that has great potential for switching protocols and topological energy transfer. So far, chiral behaviour has been intensively investigated in optical and photonic systems [26–29] while it has rarely been explored in mechanical systems because of the challenge in achieving dynamic modulations in parameter space. Until recently, chiral mode switching for mechanical vibrational modes has been realized in a time-modulated mechanical system [30]. It has been demonstrated by this study that, for chiral dynamics to occur, the starting point of the parametric loop should lie near the symmetric phase where the energy is uniformly distributed in systems. However, the symmetry-broken modes were found to undergo a dynamic evolution that is non-chiral. We note that the symmetry-broken phase corresponds to the modes with the localization of energy. Realization of the chirality of symmetry-broken modes may provide new mechanisms for unusual energy transfer manipulation.

Chiral mode switching for symmetry-broken modes was found to be relevant to the implementation of anti-parity-time (APT)-symmetric waveguide systems [31]. An APT-symmetric system, whose Hamiltonian anticommutes with the combined PT operator, represents an extension of PT-symmetric systems [32,33], and it also possesses the EP and self-intersecting eigenvalue topological Riemann surface [33–36]. Mathematically, an APT-symmetric Hamiltonian differs from a PT-symmetric one by a factor of the imaginary unit [32,34]. This results in the reversed eigenvalue topological structure between them. Such an intriguing effect makes it possible to achieve chiral mode switching for symmetry-broken modes in an APT-symmetric system. The physical realization of an APT-symmetric system is very challenging since it requires purely imaginary coupling between states [37,38]. Recently, an easy-to-implement scheme for achieving an indirect imaginary coupling was proposed in coupled optical systems by intersecting two eigenstates with an additional high-loss state [31,33,35]. By adiabatically eliminating the intermediate state, the APT symmetry has been obtained in an effective two-mode system. The extension of the idea to mechanical systems requires an exact analogy between the Schrödinger equation and Newton's equation of motion, which has not yet been deeply explored. In addition, it has remained unclear whether the chiral mode transfer of symmetry-broken modes could be realized in mechanical systems in this manner.

In this work, we investigate the construction of APT symmetry in a three-element coupled mechanical system, and implement the dynamic encircling of an APT-symmetric EP using dynamic-modulation mechanisms with time-driven stiffness. The paper is organized as follows. In §2, we first construct a mathematical analogy between the Schrödinger equation and Newton's equation of motion of a three-element system based on the tight-binding approximation. Then, the adiabatic elimination procedure is performed to create the APT symmetry in an effective two-mode system. The APT-symmetric properties and the eigenvalue topological structure in two-dimensional parameter space are analysed. In §3, the modulating structure with effective time-varying stiffness is proposed to implement the dynamic encircling of an APT-symmetric EP in parameter space. Chiral mode switching for symmetry-broken modes will be demonstrated when an APT-symmetric EP is dynamically encircled along a loop starting from the APT-broken phase. Concluding remarks are outlined in §4.

2. Construction of an APT-symmetric mechanical system

Consider two undamped oscillators with the same mass m and different spring constants k_1 and k_2. To create an imaginary coupling between these two elements, a damped oscillator with mass m, spring constant k_0 and damping coefficient c_0 is introduced to connect the undamped elements with the springs of k_L and k_R, as depicted in figure 1. Denote the displacements of the two undamped elements and the intermediate one by u_1, u_2 and u_c, respectively. The dimensionless equations of motion for each of the elements are given by

$$\left.\begin{aligned}
&\frac{\mathrm{d}^2u_1}{\mathrm{d}\tau^2}+\kappa_1u_1+\kappa_\mathrm{L}u_1-\kappa_\mathrm{L}u_\mathrm{c}=0,\\
&\frac{\mathrm{d}^2u_\mathrm{c}}{\mathrm{d}\tau^2}+\gamma_0\frac{\mathrm{d}u_\mathrm{c}}{\mathrm{d}\tau}+(1+\kappa_\mathrm{L}+\kappa_\mathrm{R})u_\mathrm{c}-\kappa_\mathrm{L}u_1-\kappa_\mathrm{R}u_2=0\\
\text{and}\qquad&\frac{\mathrm{d}^2u_2}{\mathrm{d}\tau^2}+\kappa_2u_2+\kappa_\mathrm{R}u_2-\kappa_\mathrm{R}u_\mathrm{c}=0,
\end{aligned}\right\}\tag{2.1}$$

where the normalized parameters $\kappa_1=k_1/k_0$, $\kappa_2=k_2/k_0$, $\kappa_\mathrm{L}=k_\mathrm{L}/k_0$, $\kappa_\mathrm{R}=k_\mathrm{R}/k_0$, $\gamma_0=c_0/m\omega_0$ have been used and $\tau=\omega_0t$ with $\omega_0=\sqrt{k_0/m}$. Assume harmonic solutions of the form $[u_1,u_\mathrm{c},u_2]^T=\mathbf{U}\,\mathrm{e}^{i\lambda\tau}$, where $\mathbf{U}=[\mathrm{u}_1,\mathrm{u}_\mathrm{c},\mathrm{u}_2]^T$ is a vector of oscillator amplitudes and λ refers to the eigenvalue. Equation (2.1) is expressed in matrix notation as

$$\begin{bmatrix}-\lambda^2+\beta_1+1+\kappa_\mathrm{L} & -\kappa_\mathrm{L} & 0\\ -\kappa_\mathrm{L} & -\lambda^2+i\lambda\gamma_0+1+\kappa_\mathrm{L}+\kappa_\mathrm{R} & -\kappa_\mathrm{R}\\ 0 & -\kappa_\mathrm{R} & -\lambda^2+\beta_2+1+\kappa_\mathrm{R}\end{bmatrix}\begin{bmatrix}\mathrm{u}_1\\ \mathrm{u}_\mathrm{c}\\ \mathrm{u}_2\end{bmatrix}=\mathbf{0},\tag{2.2}$$

where $\beta_1=\kappa_1-1$ and $\beta_2=\kappa_2-1$ are quantities that characterize the stiffness contrast. In order to make a connection to a quantum-mechanics system, equation (2.2) will be reformulated in a similar form to the Schrödinger equation by using the method of tight-binding approximation [15]. To this end, the presented three-element system is analysed based on an unperturbed system comprising three modes with identical oscillating frequency ω_0, while the stiffness contrast $\beta_{1,2}$, coupling spring $\kappa_{\mathrm{L,\,R}}$ and damping γ_0 are considered as small system perturbations satisfying $|\beta_{1,2}|\ll 1$, $\kappa_{\mathrm{L,\,R}}\ll 1$ and $\gamma_0\ll 1$. Under this approximation, the eigenvalue of the perturbed system (namely the studied three-element system) can be expressed as $\lambda=1+\varDelta$, where $\varDelta$ represents a small perturbation applied to the eigenvalue of the unperturbed system and satisfies $\varDelta\ll 1$. In the small-perturbation limit, $1-\lambda^2$ and $i\lambda\gamma_0$ are approximated as $-2\varDelta$ and $i\gamma_0$, respectively. Then, the eigenvalue equation for solving $\varDelta$ can be obtained as

$$\mathbf{H}_p\mathbf{U}=\varDelta\mathbf{U},\quad \text{where } \mathbf{H}_p=\frac{1}{2}\begin{bmatrix}\beta_1+\kappa_\mathrm{L} & -\kappa_\mathrm{L} & 0\\ -\kappa_\mathrm{L} & i\gamma_0+\kappa_\mathrm{L}+\kappa_\mathrm{R} & -\kappa_\mathrm{R}\\ 0 & -\kappa_\mathrm{R} & \beta_2+\kappa_\mathrm{R}\end{bmatrix}.\tag{2.3}$$

We emphasize that the Hamiltonian of the unperturbed system is represented by the 3×3 identity matrix $\mathbf{I}_3$, and $\mathbf{H}_p$ encodes all the differences of the Hamiltonian between the perturbed system and the unperturbed one [15]. Therefore, the quadratic eigenvalue problem (2.2) can be rearranged as a generic tight-binding eigenvalue relation $\mathbf{H}_{\mathrm{total}}\mathbf{U}=\lambda\mathbf{U}$, where $\mathbf{H}_{\mathrm{total}}=\mathbf{I}_3+\mathbf{H}_p$ is

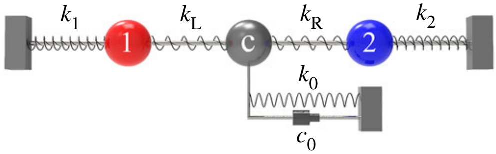

Figure 1. Schematic diagram of a coupled mass–spring resonator system with a damper attached to the middle oscillator, c. (Online version in colour.)

the Hamiltonian of the system. Using the Hamiltonian $\mathbf{H}_{\text{total}}$, the corresponding time-dependent equation is given by

$$-i\frac{\mathrm{d}}{\mathrm{d}\tau}\begin{bmatrix} v_1 \\ v_{\mathrm{c}} \\ v_2 \end{bmatrix} = \begin{bmatrix} \omega_1 & -\dfrac{\kappa_{\mathrm{L}}}{2} & 0 \\ -\dfrac{\kappa_{\mathrm{L}}}{2} & \omega_{\mathrm{c}} + i\dfrac{\gamma_0}{2} & -\dfrac{\kappa_{\mathrm{R}}}{2} \\ 0 & -\dfrac{\kappa_{\mathrm{R}}}{2} & \omega_2 \end{bmatrix}\begin{bmatrix} v_1 \\ v_{\mathrm{c}} \\ v_2 \end{bmatrix}, \tag{2.4}$$

where the complex variable $v_i (i = 1, \mathrm{c}, 2)$ is defined such that $u_i = (v_i + v_i^*)/2$, which provides a straightforward illustration of the amplitude and phase configurations of oscillator i. The modulus $|v_i|$ denotes the oscillation amplitude, while $\mathrm{Re}(v_i)$ represents the instantaneous response u_i. Note that $\omega_1 = 1 + (\beta_1 + \kappa_{\mathrm{L}})/2$, $\omega_{\mathrm{c}} = 1 + (\kappa_{\mathrm{L}} + \kappa_{\mathrm{R}})/2$ and $\omega_2 = 1 + (\beta_2 + \kappa_{\mathrm{R}})/2$ refer to the normalized natural frequencies of the three oscillators after perturbation, and $-\kappa_{\mathrm{L,\,R}}/2$ denotes the coupling between adjacent ones.

Next, we perform the adiabatic elimination procedure [39–41] for the lossy oscillator c in order to construct the APT symmetry in an effective two-mode system. Introduce auxiliary fields $\tilde{v}_i$ $(i = 1, \mathrm{c}, 2)$, which satisfy $v_i(\tau) = \tilde{v}_i(\tau)\exp(i\omega_i\tau)$. Equation (2.4) can be rewritten in terms of the fields $\tilde{v}_i$ by

$$-i\frac{\mathrm{d}}{\mathrm{d}\tau}\begin{bmatrix} \tilde{v}_1 \\ \tilde{v}_{\mathrm{c}} \\ \tilde{v}_2 \end{bmatrix} = \begin{bmatrix} 0 & -\dfrac{\kappa_{\mathrm{L}}}{2}e^{-i\Delta\omega_1\tau} & 0 \\ -\dfrac{\kappa_{\mathrm{L}}}{2}\mathrm{e}^{i\Delta\omega_1\tau} & i\dfrac{\gamma_0}{2} & -\dfrac{\kappa_{\mathrm{R}}}{2}\mathrm{e}^{i\Delta\omega_2\tau} \\ 0 & -\dfrac{\kappa_{\mathrm{R}}}{2}\mathrm{e}^{-i\Delta\omega_2\tau} & 0 \end{bmatrix}\begin{bmatrix} \tilde{v}_1 \\ \tilde{v}_{\mathrm{c}} \\ \tilde{v}_2 \end{bmatrix}, \tag{2.5}$$

where $\Delta\omega_1 = \omega_1 - \omega_{\mathrm{c}}$ and $\Delta\omega_2 = \omega_2 - \omega_{\mathrm{c}}$. Assuming a sufficiently large damping ratio $\gamma_0 \gg \kappa_{\mathrm{L}}, \kappa_{\mathrm{R}}$, we have $\mathrm{d}\tilde{v}_c/\mathrm{d}\tau \approx -(\gamma_0/2)\tilde{v}_c \gg \mathrm{d}\tilde{v}_1/\mathrm{d}\tau, \mathrm{d}\tilde{v}_2/\mathrm{d}\tau$ according to equation (2.5). The inequality means that the variable $\tilde{v}_{\mathrm{c}}$ varies in time very rapidly in comparison with $\tilde{v}_1$ and $\tilde{v}_2$. Therefore, $\tilde{v}_{\mathrm{c}}$ is categorized as the fast variable and will decrease drastically with decay rate $\gamma_0/2$. By contrast, variables $\tilde{v}_{1,2}$ are slow ones that evolve over a much longer time period before reaching a steady state. By integrating the second equation in (2.5) with respect to time, the general expression of the fast variable $\tilde{v}_{\mathrm{c}}$ is given by [33,41]

$$\begin{aligned} \tilde{v}_{\mathrm{c}}(\tau) = &-i\frac{\kappa_{\mathrm{L}}}{2}\int_0^{\tau}\tilde{v}_1(\tau-\tau')\mathrm{e}^{i\Delta\omega_1(\tau-\tau')}\mathrm{e}^{-(\gamma_0/2)\tau'}\,\mathrm{d}\tau' \\ &-i\frac{\kappa_{\mathrm{R}}}{2}\int_0^{\tau}\tilde{v}_2(\tau-\tau')\mathrm{e}^{i\Delta\omega_2(\tau-\tau')}\mathrm{e}^{-(\gamma_0/2)\tau'}\,\mathrm{d}\tau', \end{aligned} \tag{2.6}$$

where we have set $\tilde{v}_{\mathrm{c}}(0) = 0$ at the initial time $\tau = 0$. Since $\gamma_0/2$ is extremely large, the mean lifetime of the exponentially decaying term $\exp(-(\gamma_0/2)\tau')$ is close to zero. Thereby, slow variables $\tilde{v}_1$ and $\tilde{v}_2$ satisfy the approximate relationship $\tilde{v}_{1,2}(\tau-\tau')\exp(-(\gamma_0/2)\tau') \approx \tilde{v}_{1,2}(\tau)\exp(-(\gamma_0/2)\tau')$ for $0 \le \tau' \le \tau$. Equation (2.6) is then simplified as

$$\tilde{v}_{\mathrm{c}}(\tau) = -i\frac{\kappa_{\mathrm{L}}}{2}\tilde{v}_1(\tau)\int_0^{\tau}\mathrm{e}^{i\Delta\omega_1(\tau-\tau')}\mathrm{e}^{-(\gamma_0/2)\tau'}\,\mathrm{d}\tau' - i\frac{\kappa_{\mathrm{R}}}{2}\tilde{v}_2(\tau)\int_0^{\tau}\mathrm{e}^{i\Delta\omega_2(\tau-\tau')}\mathrm{e}^{-(\gamma_0/2)\tau'}\,\mathrm{d}\tau'. \tag{2.7}$$

Considering that τ measures the time scale of slow variables following $\tau \gg 2/\gamma_0$, equation (2.7) is further given by

$$\tilde{v}_c(\tau) = -\frac{i\kappa_L}{2(i\Delta\omega_1 + \gamma_0/2)}\tilde{v}_1(\tau)e^{i\Delta\omega_1\tau} - \frac{i\kappa_R}{2(i\Delta\omega_2 + \gamma_0/2)}\tilde{v}_2(\tau)e^{i\Delta\omega_2\tau}. \tag{2.8}$$

By substituting equation (2.8) into (2.5), the fast variable $\tilde{v}_c(\tau)$ can be adiabatically eliminated, and then the equation that governs the evolution of slow variables $\tilde{v}_1$ and $\tilde{v}_2$ is given by

$$-i\frac{d}{d\tau}\begin{bmatrix}\tilde{v}_1\\ \tilde{v}_2\end{bmatrix} = \begin{bmatrix} i\Gamma_{11} & i\Gamma_{12}e^{-i(\omega_1-\omega_2)\tau}\\ i\Gamma_{21}e^{i(\omega_1-\omega_2)\tau} & i\Gamma_{22}\end{bmatrix}\begin{bmatrix}\tilde{v}_1\\ \tilde{v}_2\end{bmatrix}, \tag{2.9}$$

where

$$\Gamma_{11} = \frac{\kappa_L^2}{4i\Delta\omega_1 + 2\gamma_0}, \Gamma_{22} = \frac{\kappa_R^2}{4i\Delta\omega_2 + 2\gamma_0}, \Gamma_{12} = \frac{\kappa_L\kappa_R}{4i\Delta\omega_2 + 2\gamma_0}, \Gamma_{21} = \frac{\kappa_L\kappa_R}{4i\Delta\omega_1 + 2\gamma_0}.$$

In terms of the complex variable v_i, equation (2.9) is rewritten as

$$-i\frac{d}{d\tau}\begin{bmatrix}v_1\\ v_2\end{bmatrix} = \begin{bmatrix} \omega_1 + i\Gamma_{11} & i\Gamma_{12}\\ i\Gamma_{21} & \omega_2 + i\Gamma_{22}\end{bmatrix}\begin{bmatrix}v_1\\ v_2\end{bmatrix}, \tag{2.10}$$

where Γ_{11}, Γ_{22} characterize the loss rate of two oscillators and Γ_{12}, Γ_{21} refer to the mode coupling coefficient. We further assume that $|\Delta\omega_{1,2}| \ll \gamma_0/2$ and $\kappa_L = \kappa_R = \kappa$. Under this condition, the coupled mode equation (2.10) is given by

$$-i\frac{d}{d\tau}\begin{bmatrix}v_1\\ v_2\end{bmatrix} = \begin{bmatrix} \alpha_{ave} + \alpha_{dif} + i\Gamma & i\Gamma\\ i\Gamma & \alpha_{ave} - \alpha_{dif} + i\Gamma\end{bmatrix}\begin{bmatrix}v_1\\ v_2\end{bmatrix}, \tag{2.11}$$

where $\alpha_{ave} = (\omega_1 + \omega_2)/2$, $\alpha_{dif} = (\omega_1 - \omega_2)/2$ and $\Gamma = \kappa^2/(2\gamma_0)$. Equation (2.11) gives the evolution over time of slow variables pertaining to two undamped oscillators. To confirm that the effective two-mode system described by equation (2.11) is APT-symmetric, we perform the gauge transformation $\boldsymbol{\varphi} = e^{-i\alpha_{ave}\tau}[v_1, v_2]^T$ for equation (2.11), obtaining that

$$-i\frac{d\boldsymbol{\varphi}}{d\tau} = \mathbf{H}_{APT}\boldsymbol{\varphi}, \quad \text{where } \mathbf{H}_{APT} = \begin{bmatrix}\alpha_{dif} + i\Gamma & i\Gamma\\ i\Gamma & -\alpha_{dif} + i\Gamma\end{bmatrix}. \tag{2.12}$$

Equation (2.12) is similar in form to the Schrödinger equation in quantum-mechanics systems. The Hamiltonian $\mathbf{H}_{APT}$ of this two-level system is characterized by the fact that two oscillators attenuate at equal decay rate Γ, but differ in their natural frequencies by $2\alpha_{dif}$. Meanwhile, the coupling constant $i\Gamma$ of these two modes is purely imaginary. It is known that the time-reversal operator T flips the direction of time evolution and returns its complex conjugation when acting on the Hamiltonian [42]. The parity operator P refers to the space inversion operation described by the Pauli matrix $\sigma_x = [\begin{smallmatrix}0 & 1\\ 1 & 0\end{smallmatrix}]$ [3,43]. Under the combined P and T operation, it is readily found that the Hamiltonian $\mathbf{H}_{APT}$ of the form (2.12) satisfies the APT-symmetric relationship

$$(PT)\mathbf{H}_{APT}(PT)^{-1} = -\mathbf{H}_{APT}. \tag{2.13}$$

By contrast, a PT-symmetric Hamiltonian $\mathbf{H}_{PT}$ with the relation of $\mathbf{H}_{APT} = i\mathbf{H}_{PT}$ is invariant under the combined parity and time-reversal operation, satisfying $(PT)\mathbf{H}_{PT}(PT)^{-1} = \mathbf{H}_{PT}$.

Now let us revisit equation (2.11) and denote the system's eigenvector by $\boldsymbol{\psi} = [v_1, v_2]^T$ and the corresponding eigenvalue by λ. By solving the model Hamiltonian in equation (2.11), we can get two sets of eigenstate solutions

$$\lambda_{1,2} = \alpha_{ave} + i\Gamma \mp \sqrt{\alpha_{dif}^2 - \Gamma^2}, \quad \boldsymbol{\psi}_{1,2} = \left[-i\frac{\left(\alpha_{dif} \mp \sqrt{\alpha_{dif}^2 - \Gamma^2}\right)}{\Gamma}, 1\right]. \tag{2.14}$$

In the case of $\Gamma/\alpha_{dif} > 1$, we see from equation (2.14) that the real parts of two eigenvalues coalesce while the imaginary parts are split. In addition, each eigenvector is invariant under simultaneous

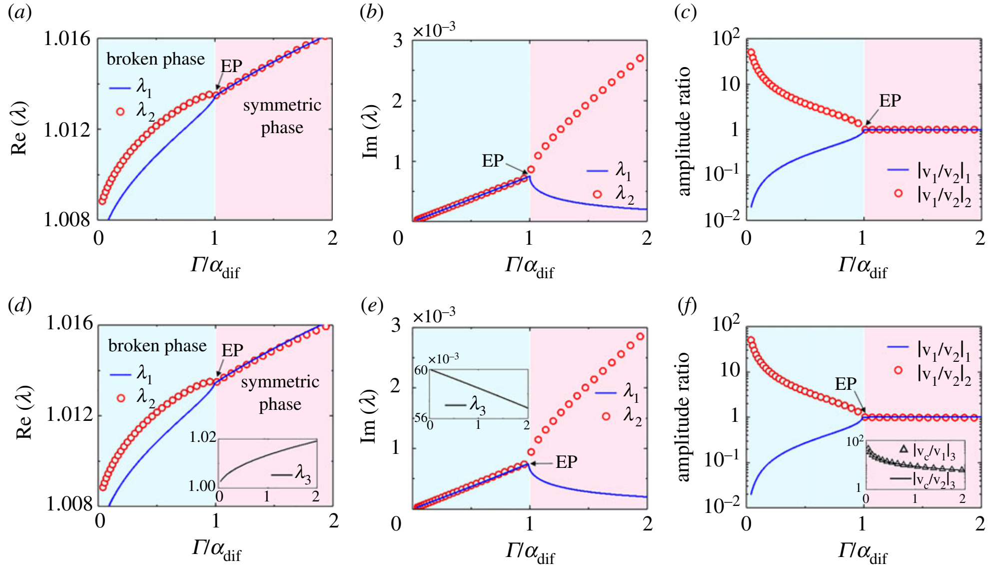

Figure 2. The eigenvalue and modal amplitude ratio of the effective two-mode system (*a*–*c*) and original three-element system (*d*–*f*). The real parts (*a*,*d*) and imaginary parts (*b*,*e*) of the eigenvalues; (*c*,*f*) the amplitude ratio of the eigenmodes. The insets show the results of mode 3. (Online version in colour.)

P and T operations, i.e. $PT\boldsymbol{\psi}_{1,2} = \boldsymbol{\psi}_{1,2}$, and exhibits the balanced field profiles $|\mathrm{v}_1/\mathrm{v}_2|_{1,2} = 1$. These are the important characteristics of the APT-symmetric phase. When $\Gamma/\alpha_{\mathrm{dif}} < 1$, the two eigenvalues have the same imaginary parts but different real parts instead. In this regime, the PT operation transforms one eigenvector into the other as given by $PT\boldsymbol{\psi}_{1,2} = \boldsymbol{\psi}_{2,1}$. This leads to an asymmetric amplitude ratio distribution ($|\mathrm{v}_1/\mathrm{v}_2|_1 = |\mathrm{v}_2/\mathrm{v}_1|_2 > 1$), which means that the eigenmode field is always localized to one oscillator. This is the landmark effect of the APT-broken phase. In between these two phases, there is a threshold condition, $\Gamma/\alpha_{\mathrm{dif}} = 1$, at which both eigenvalues and the corresponding eigenvectors become degenerate. Here, this non-Hermitian degenerate point is termed the APT-symmetric EP in order to distinguish itself from the EP occurring in PT-symmetric systems.

Figure 2*a*–*c* shows the quantitative results of the evolution of the eigenvalues and modal amplitude ratio against $\Gamma/\alpha_{\mathrm{dif}}$ by varying the coupling strength κ, which are calculated according to equation (2.14) using parameters $\kappa_1 = 1.015$, $\kappa_2 = 1.012$ and $\gamma_0 = 0.12$. In the region beyond $\Gamma/\alpha_{\mathrm{dif}} = 1$ is the APT-symmetric phase, which predicts the uniform motion distribution in the stationary state of systems. For further illustration, taking $\Gamma/\alpha_{\mathrm{dif}} = 1.5$ and initial conditions $[v_1, v_2] = [0, 1]$ at $\tau = 0$, the time-dependent responses of field amplitudes $|v_1|$ and $|v_2|$ are computed by solving equation (2.11), as shown in figure 3*a*. Oscillator 2 quickly transfers its energy to oscillator 1, and they later tend to move with nearly equal amplitude $|v_1/v_2| \simeq 1$ as protected by the APT symmetry. In another example, we choose $\Gamma/\alpha_{\mathrm{dif}} = 0.5$, which falls within the regime of the APT-broken phase. The corresponding time evolutions of the field amplitudes under the same initial conditions are shown in figure 3*b*. The energy cyclically flows back and forth between two oscillators, and does not tend to be evenly distributed owing to the fluctuation of $|v_1/v_2|$. This is consistent with the prediction by the APT-broken phase.

It is worthy of note that the field responses of the effective two-mode system would be predicted to coincide with those retrieved from the original three-element system, as guaranteed by the adiabatic elimination concept. For verification, using equation (2.4) we calculate the eigenvalues and modal amplitude ratio of the three-element system as plotted in figure 2*d*–*f*. Excellent agreement can be observed when compared with the results in figure 2*a*–*c*. Figure 3*c*,*d*

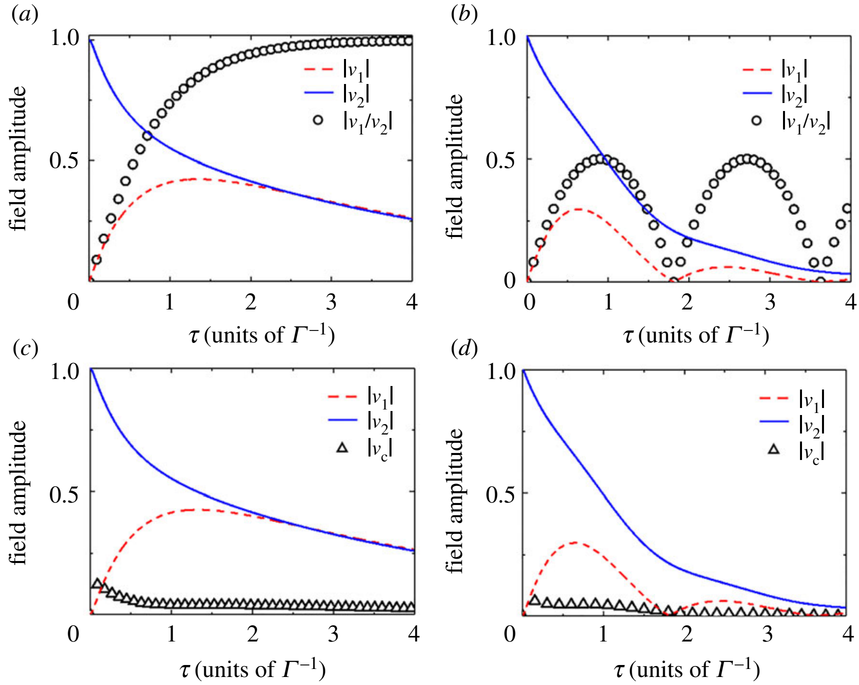

Figure 3. Time-dependent field responses of the effective two-mode system (*a*,*b*) and original three-element system (*c*,*d*). Field responses of the APT-symmetric phase with $\Gamma/\alpha_{\rm dif} = 1.5$ (*a*,*c*) and the symmetry-broken phase with $\Gamma/\alpha_{\rm dif} = 0.5$ (*b*,*d*). (Online version in colour.)

presents the time-dependent field responses of the original system under the same conditions as figure 3*a*,*b*. The effectiveness of the adiabatic elimination can again be verified by the coincidence of the temporal responses between the two systems. In the insets of figure 2*d*–*f*, a decoupled mode with localized fields at lossy oscillator c ($|v_c/v_{1,2}|_3 \gg 1$) is shown to possess a significantly larger damping factor than the other eigenmodes. As a result, the oscillating amplitude of oscillator c cannot build up significantly and thus remains as its initial value ($|v_c(\tau)| \approx |v_c(\tau = 0)|$), as demonstrated in figure 3*c*,*d*. Thereby, the intermediate oscillator c can be adiabatically eliminated without significantly altering the dynamics of the outer oscillators. The above results show that the dynamic evolution of the symmetric and symmetry-broken phases in the original three-element system can be accurately captured by the effective two-mode system with the help of adiabatic elimination, which can then be used to provide a precise prediction of the APT-symmetric EP. This is critical to the construction of the APT-symmetric mechanical system.

3. Mode switching by dynamically encircling the APT-symmetric EP

Let us examine the topological structure of eigenvalues in the two-dimensional parameter space (κ_L, κ_R) for the three-element system with parameters $\kappa_1 = 1.015$, $\kappa_2 = 1.012$ and $\gamma_0 = 0.12$. The EP occurs at $\Gamma/\alpha_{\rm dif} = 1$, which predicts the point of $\kappa_L = \kappa_R = 0.0134$, which we denote by $\kappa_{\rm EP}$. In the vicinity of the EP, the real and imaginary parts of eigenvalues against the variation of κ_L and κ_R are shown in figure 4*a*,*b*, respectively. The system is shown to possesses three eigenstates; according to the magnitude of mode damping (i.e. imaginary parts of eigenvalues), they are termed here as modes 1, 2 and 3 with low, high and extremely high losses, respectively. Constrained by the adiabatic elimination, mode 3 localized at the lossy oscillator c has been successfully removed away from the other modes. As a result, one can observe clearly the self-intersecting Riemann

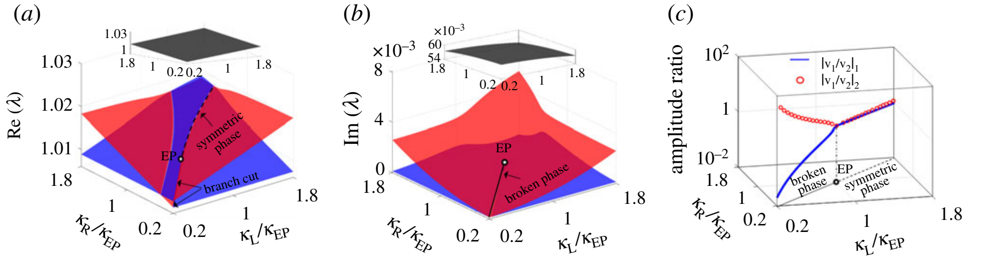

Figure 4. (*a*) Real and (*b*) imaginary parts of eigenvalues in the two-dimensional parameter space ($\kappa_{\mathrm{L}}, \kappa_{\mathrm{R}}$); (*c*) the distribution of the amplitude ratio of modal fields for modes 1 and 2 on the lines of the APT-symmetric phase and APT-broken phase. (Online version in colour.)

sheets relevant to the low-loss and high-loss states. The eigenmode evolution around the EP on the Riemann sheets will be covered in this section.

Figure 4*c* shows the amplitude ratio of the modal fields of modes 1 and 2 on the line where either real or imaginary parts of eigenvalues coalesce. Consistent with the observation in figure 2, it is found that the APT-broken phase occurs at the branch cut (BC) line where the imaginary parts of the eigenvalues coalesce (solid line) while the real parts of the eigenvalues bifurcate, resulting in the fact that mode 1 is mostly localized in oscillator 2 and mode 2 in oscillator 1. The coalescing of real parts of eigenvalues (dashed line) corresponds to the APT-symmetric phase, which ensures the nearly equal distribution of energy between two oscillators. We emphasize that the topological structure of eigenvalues near the APT-symmetric EP has been reversed in contrast to the PT-symmetric system. In the latter, the imaginary parts of eigenvalues coalesce for the PT-symmetric phase while the real parts coalesce for the broken PT-symmetric phase [2,3]. According to this reversed symmetry effect, we may expect that the chiral mode switching by the dynamic encircling of the EP, which in PT-symmetric systems appears for symmetric and anti-symmetric modes [30], would be observed for symmetry-broken modes in the APT-symmetric systems.

When we consider the dynamic encircling of an EP, the non-Hermitian Hamiltonian should be modulated as being time-dependent to generate the time evolution of eigenstates. This requires the continuous changing of κ_{L} and κ_{R} with time along a controlled path encircling the EP. In our previous study [30], the dynamic-mechanism metamaterials were employed for time modulation of the ground stiffness and viscosity, and they allowed for easy tuning of the starting/end points and encircling direction of the parametric loop. Here, the concept of the dynamic-modulation mechanism is used again to design the time-varying stiffness κ_{L} and κ_{R}. Figure 5*a* shows the modulating structure that is capable of dynamic encircling of an EP, where adjacent rigid bodies are connected with a pair of perpendicularly arranged springs that rotate about an axis vertical to the main track. The two mechanisms rotate with the same angular frequency Ω_r from initial biasing angles Φ_0 and Ψ_0. Through the homogenization analysis [30,44], the two rotary-spring mechanisms can be effectively represented by springs with time-varying stiffness $\kappa_{\mathrm{L}}(\tau)$ and $\kappa_{\mathrm{R}}(\tau)$, as given by

$$\kappa_{\mathrm{L}}(\tau) = \kappa_{\mathrm{L}}^0 + \kappa_{\mathrm{L}}^1 \cos 2\Phi(\tau) \quad \text{and} \quad \kappa_{\mathrm{R}}(\tau) = \kappa_{\mathrm{R}}^0 + \kappa_{\mathrm{R}}^1 \cos 2\Psi(\tau), \tag{3.1}$$

where $\kappa_{\mathrm{L}}^0 = (k_3 + k_5 + k_6)/k_0$, $\kappa_{\mathrm{L}}^1 = (k_5 - k_6)/k_0$, $\kappa_{\mathrm{R}}^0 = (k_4 + k_7 + k_8)/k_0$ and $\kappa_{\mathrm{R}}^1 = (k_7 - k_8)/k_0$. $\Phi(\tau) = \Phi_0 \pm \omega_r \tau$ and $\Psi(\tau) = \Psi_0 \pm \omega_r \tau$ are phase angles at a certain time τ with $\omega_r = \Omega_r/\omega_0$, and the '+' and '−' notation denotes the anti-clockwise and clockwise rotation of rotary-spring mechanisms, respectively. By incorporating time-varying parameters $\kappa_{\mathrm{L}}(\tau)$ and $\kappa_{\mathrm{R}}(\tau)$ into equation (2.4), the

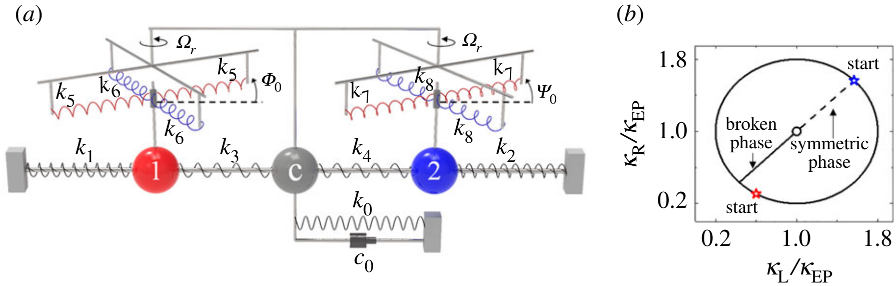

Figure 5. (*a*) Schematic diagram of the modulated structure containing dynamic mechanisms; (*b*) Parametric loop enclosing the EP parameterized by equation (3.1). The circle and star symbols mark the starting point and EP, respectively. (Online version in colour.)

formulation that predicts the time evolution of eigenstates is written as

$$-i\frac{\mathrm{d}}{\mathrm{d}\tau}\begin{bmatrix} v_1 \\ v_\mathrm{c} \\ v_2 \end{bmatrix} = \mathbf{H}_\mathrm{total}(\tau)\begin{bmatrix} v_1 \\ v_\mathrm{c} \\ v_2 \end{bmatrix}, \tag{3.2}$$

where the time-dependent Hamiltonian is given by

$$\mathbf{H}_\mathrm{total}(\tau) = \begin{bmatrix} 1+\dfrac{\beta_1+\kappa_\mathrm{L}(\tau)}{2} & -\dfrac{\kappa_\mathrm{L}(\tau)}{2} & 0 \\ -\dfrac{\kappa_\mathrm{L}(\tau)}{2} & 1+\dfrac{i\gamma_0+\kappa_\mathrm{L}(\tau)+\kappa_\mathrm{R}(\tau)}{2} & -\dfrac{\kappa_\mathrm{R}(\tau)}{2} \\ 0 & -\dfrac{\kappa_\mathrm{R}(\tau)}{2} & 1+\dfrac{\beta_2+\kappa_\mathrm{R}(\tau)}{2} \end{bmatrix}. \tag{3.3}$$

To evaluate the eigenmode evolution in the process of the dynamic encircling of an APT-symmetric EP, we first solve the time-dependent equation (3.2) under initial conditions, then we expand the displacement response $\mathbf{v}(\tau) = [v_1, v_\mathrm{c}, v_2]^T$ at each time τ as a sum of the instantaneous eigenvectors, i.e. $\mathbf{v}(\tau) = p_1\mathbf{z}_1 + p_2\mathbf{z}_2 + p_3\mathbf{z}_3$. Note that p_i refers to the instantaneous modal amplitude of mode i, and $\mathbf{z}_i$ is the right eigenvector of the eigenvalue problem $\mathbf{H}_\mathrm{total}\mathbf{z}_i = \lambda_i\mathbf{z}_i$. Since $\mathbf{H}_\mathrm{total}$ is non-Hermitian, the right eigenvectors are typically not orthogonal, namely $\mathbf{z}_i^\dagger\mathbf{z}_j \neq \delta_{i,j}$, where † represents the Hermitian conjugate operation and $\delta_{i,j}$ is the Kronecker delta. However, by constructing the left eigenvectors $\mathbf{l}_i$ as defined by $\mathbf{H}_\mathrm{total}^\dagger\mathbf{l}_i = \lambda_i^*\mathbf{l}_i$, we have the biorthogonal relationship $\mathbf{l}_i^\dagger\mathbf{z}_j = \delta_{i,j}$ [45]. Finally, the unknown amplitude p_i can be determined by $p_i = \mathbf{l}_i^\dagger\mathbf{v}(\tau)$ [46], and can be used to disclose the eigenmode evolution behaviour [29,31].

Consider parameters $\kappa_\mathrm{L}^0 = \kappa_\mathrm{R}^0 = \kappa_\mathrm{EP}$, $\kappa_\mathrm{L}^1 = \kappa_\mathrm{R}^1 = 0.8\kappa_\mathrm{EP}$ and $\omega_r = 0.002$. To excite the evolution of the symmetry-broken state, we set the starting point near the APT-broken phase by choosing initial phase angles $\Phi_0 = 2\pi/3$ and $\Psi_0 = 5\pi/12$. The loop trajectory formed from phase functions $\Phi(\tau) = 2\pi/3 \pm \omega_r\tau$ and $\Psi(\tau) = 5\pi/12 \pm \omega_r\tau$ has been shown in figure 5*b*, where the spinning direction '+' ('−') of rotary mechanisms determines the anti-clockwise (clockwise) evolution along the parametric loop. When a pure mode 1 or mode 2 is injected into the system as the initial excitation, we are now interested in which one of the modes would dominate after a complete evolution along the loop in various cases of input states and encircling directions. Chiral dynamics of symmetry-broken states can then be identified in this way.

Figure 6*e* plots the variation in the modal amplitudes of all three modes when we input mode 1 and examine the anticlockwise encircling of the EP. The corresponding evolution trajectories are drawn on the Riemann sheets, as shown in figure 6*a*. Mode 1 is seen to experience a stable and adiabatic evolution on the low-loss Riemann sheet, and it always dominates until going across the BC where the imaginary parts of eigenvalues coalesce, resulting in the exchange of mode

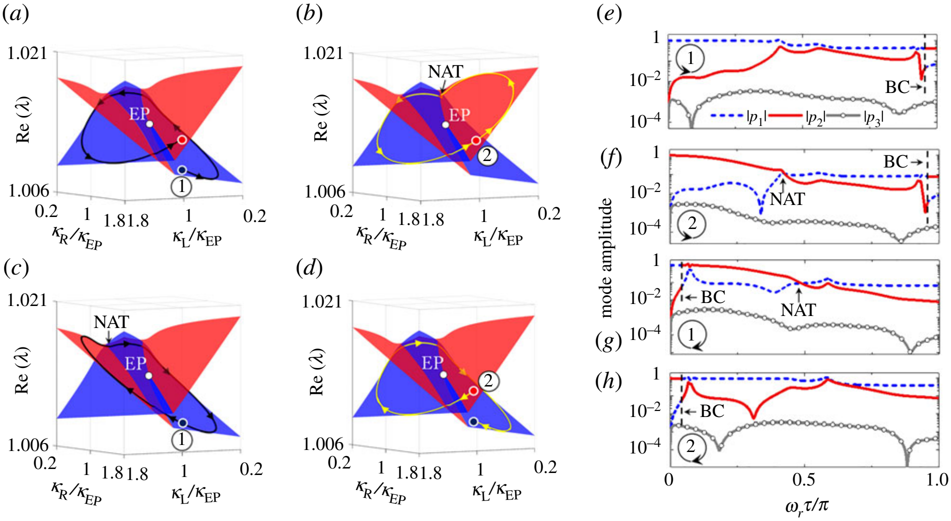

Figure 6. (*a*–*d*) Eigenstate evolution trajectories drawn on Riemann sheets and (*e*–*h*) time evolution of the modal amplitudes when the APT-symmetric EP is encircled along the loop with the starting point near the APT-broken phase in four different cases of the input state and loop orientation: (*a*,*e*) mode 1 input and anti-clockwise orientation; (*b*,*f*) mode 2 input and anti-clockwise orientation; (*c*,*g*) mode 1 input and clockwise orientation; (*d*,*h*) mode 2 input and clockwise orientation. (Online version in colour.)

identity. Eventually, the system outputs mode 2 owing to the fact that $|p_2| > |p_1| > |p_3|$. Figure 6*b*,*f* shows the corresponding results for mode 2 as the input state. The mode 2 that propagates on the high-loss Riemann sheet is seen to excite the low-loss mode 1 because of the non-adiabatic coupling [25,47]. Mode 1 would become dominant after passing through the crossing point of amplitude curves in figure 6*f*. On the Riemann surface (figure 6*b*), this point is characterized by an abrupt jump from the high-loss sheet to the low-loss sheet [30], which is known as the NAT. Note that the occurrence of the NAT is required by the system stability, and it is related to the more general phenomenon of stability loss delay in dynamical bifurcations [46,48]. After experiencing the NAT, the dominant state would return to mode 2 owing to the BC, which keeps dominating until the end of the evolution.To sum up, the system always outputs mode 2 for the anti-clockwise encircling, regardless of the input states. For the clockwise encircling case, mode 1, when inputted into the system, will be transformed to the high-loss mode 2 by the BC, as shown in figure 6*c*,*g*. After some delay the NAT occurs, resulting in the eigenstate returning the low-loss sheet, and mode 1 dominates until the end of the loop. When mode 2 is injected, figure 6*d*,*h* shows that the dominant state is soon changed to mode 1 owing to the BC, which later evolves stably on the low-loss Riemann sheet without the occurrence of the NAT. In these two cases, the output state is always mode 1. In all cases mentioned above, the modal amplitude of mode 3 has also been shown, and it is two orders of magnitude smaller than that of the dominant states. Thus, its effect on the evolution of the other two modes is minor.

Based on the above observation, we can conclude that the chiral mode switching, which states that the output state is controlled mainly by the encircling direction while it is irrelevant to the input states, has been achieved for symmetry-broken states. In fact, the chiral dynamics of eigenmodes originates from the special topology of eigenvalue Riemann surfaces, and is a general feature in non-Hermitian systems. To create the chirality, the parametric loop must start from a point where the two eigenmodes carry nearly the same losses (imaginary parts of eigenvalues). In PT-symmetric systems, the PT-symmetric phase locates at the line where imaginary parts of eigenvalues coalesce, therefore the symmetric-phase mode exhibits the chiral switching behaviour [29,30], whereas in the APT-symmetric systems studied here that line

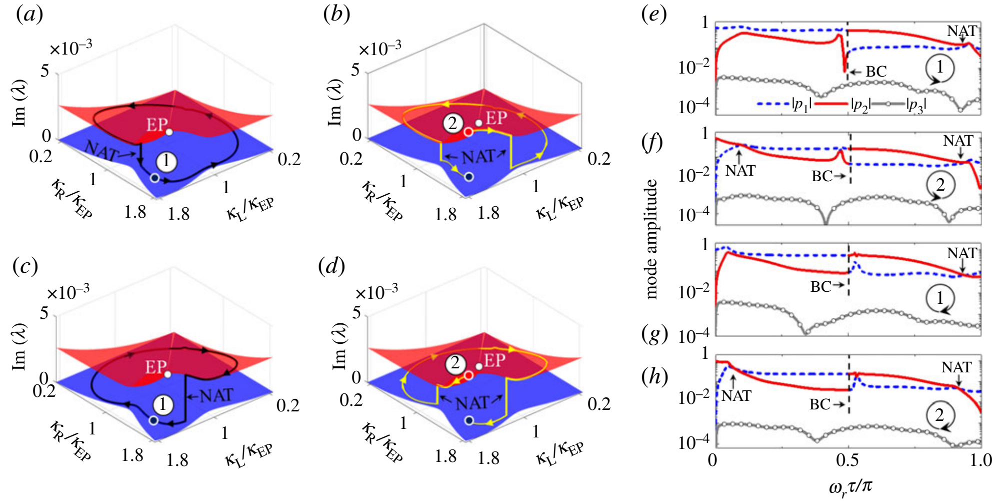

Figure 7. (*a–d*) Eigenstate evolution trajectories drawn on Riemann sheets and (*e–h*) modal amplitudes when the APT-symmetric EP is encircled along the loop with the starting point near the APT-symmetric phase in four different cases of the input state and loop orientation: (*a*,*e*) mode 1 input and anti-clockwise orientation; (*b*,*f*) mode 2 input and anti-clockwise orientation; (*c*,*g*) mode 1 input and clockwise orientation; (*d*,*h*) mode 2 input and clockwise orientation. (Online version in colour.)

is the symmetry-broken phase, as has been illustrated in figure 2. Hence, the evolution of symmetry-broken states becomes chiral.

We may question the evolution behaviour of symmetric-phase modes in APT-symmetric systems. To clarify this issue, we investigate the state evolution for encircling loops with starting points at the symmetric phase by setting phase functions as $\Phi(\tau) = \pi/8 \pm \omega_r\tau$ and $\Psi(\tau) = 7\pi/8 \pm \omega_r\tau$, as shown in figure 5*b* for the corresponding loop trajectory. For the low-loss mode 1 injection, figure 7*a*,*e* shows the anti-clockwise encircling case, where it is seen that mode 1 undergoes stable evolution on the low-loss Riemann sheet until entering the high-loss Riemann sheet upon passing through the BC line. The NAT then occurs, causing the state to jump back to the low-loss sheet; later, the state evolution becomes stable for the rest of the loop. The dynamical process is more complicated for mode 2 injection (figure 7*b*,*f*). The system undergoes the NAT twice and the BC-induced mode switching once, and finally outputs mode 1. For the clockwise encircling case, the evolution behaviour under different input states is quite similar to the scenario of anti-clockwise loops. For all four cases shown in figure 7, the output state is always the low-loss mode 1 regardless of the input states and encircling direction. Here, the system reveals the non-chiral behaviour, which is completely different from the chiral dynamics appearing when the APT-symmetric EP is encircled with the starting point lying near the symmetry-broken phase. The underlying mechanism can be attributed to the distinct topological structure of the eigenvalue Riemann surfaces in different parametric regions.

4. Conclusion

In this paper, we investigate the mode-switching effect achieved by dynamic encircling of an EP in an APT-symmetric mechanical system consisting of three oscillators with a damper attached to the middle one. The APT symmetry is obtained in the effective two-mode system by performing an adiabatic elimination procedure for the intermediate lossy oscillator. As guaranteed by the adiabatic elimination, the field responses of the effective two-mode system are demonstrated to coincide excellently with those retrieved from the original three-element system. In the effective two-mode system, we have observed the APT-symmetric EP, and the topological structure of eigenvalues near the EP has been reversed in contrast to the PT-symmetric system.

The dynamic encircling of the APT-symmetric EP is realized in the dynamic-modulation system, which consists of three sets of mass–spring resonators that are coupled through two rotating spring mechanisms. We show that the rotary mechanisms can be effectively represented by springs with time-varying stiffness, which could drive the time evolution of eigenstates along a path encircling the EP in the parameter space. Based on the proposed time-modulating structure, we have observed the chiral dynamics of symmetry-broken modes when the APT-symmetric EP is dynamically encircled along a parametric loop with the starting point lying near the symmetry-broken phase, while the non-chiral behaviour is found for APT-symmetric modes. These dynamic behaviours have been reversed in comparison with PT-symmetric systems. The underlying mechanism originates from distinct topological structures of eigenvalue Riemann surfaces between PT-symmetric and APT-symmetric systems. The present study is expected to open up new schemes towards unprecedented manipulation of coupled wave and vibrational modes in mechanical systems with APT-symmetric EPs.

Data accessibility. The paper contains no experimental data. All results and illustrative computations are directly reproducible. The information and codes to reproduce the results of this article are provided in the paper and the electronic supplementary material.

Authors' contributions. L.G. and X.M.Z. conceived the core concept and mathematical model. L.G. derived the analytical results and carried out the numerical simulations. W.Z. and X.D.Z. participated in the design of the study. All authors discussed the results and commented on the manuscript. All authors approved the final version and agree to be held accountable for all aspects of the work.

Competing interests. We declare we have no competing interests.

Funding. This work was supported by the National Natural Science Foundation of China (11872111, 11991030, 11991033 and 11622215); 111 project (B16003) and the National Key R & D Program of China under grant no. 2017YFA0303800.

References

1. Rotter I. 2009 A non-Hermitian Hamilton operator and the physics of open quantum systems. *J. Phys. A: Math. Theor.* **42**, 153001. (doi:10.1088/1751-8113/42/15/153001)
2. El-Ganainy R, Makris KG, Khajavikhan M, Musslimani ZH, Rotter S, Christodoulides DN. 2018 Non-Hermitian physics and PT symmetry. *Nat. Phys.* **14**, 11–19. (doi:10.1038/nphys4323)
3. Özdemir ŞK, Rotter S, Nori F, Yang L. 2019 Parity-time symmetry and exceptional points in photonics. *Nat. Mater.* **18**, 783–798. (doi:10.1038/s41563-019-0304-9)
4. Kato T. 1966 *Perturbation theory for linear operators*. Germany: Springer: Berlin.
5. Miri MA, Alù A. 2019 Exceptional points in optics and photonics. *Science* **363**, eaar7709. (doi:10.1126/science.aar7709)
6. Lin Z, Ramezani H, Eichelkraut T, Kottos T, Cao H, Christodoulides DN. 2011 Unidirectional invisibility induced by PT-symmetric periodic structures. *Phys. Rev. Lett.* **106**, 213901. (doi:10.1103/PhysRevLett.106.213901)
7. Feng L, Xu YL, Fegadolli WS, Lu MH, Oliveira JE, Almeida VR, Chen YF, Scherer A. 2013 Experimental demonstration of a unidirectional reflectionless parity-time metamaterial at optical frequencies. *Nat. Mater.* **12**, 108–113. (doi:10.1038/nmat3495)
8. Peng B, Özdemir ŞK, Rotter S, Yilmaz H, Liertzer M, Monifi F, Bender CM, Nori F, Yang L. 2014 Loss-induced suppression and revival of lasing. *Science* **346**, 328–332. (doi:10.1126/science.1258004)
9. Wiersig J. 2014 Enhancing the sensitivity of frequency and energy splitting detection by using exceptional points: application to microcavity sensors for single-particle detection. *Phys. Rev. Lett.* **112**, 203901. (doi:10.1103/PhysRevLett.112.203901)
10. Chen W, Özdemir ŞK, Zhao G, Wiersig J, Yang L. 2017 Exceptional points enhance sensing in an optical microcavity. *Nature* **548**, 192–196. (doi:10.1038/nature23281)
11. Zhu X, Ramezani H, Shi C, Zhu J, Zhang X. 2014 PT-symmetric acoustics. *Phys. Rev. X* **4**, 031042. (doi:10.1103/PhysRevX.4.031042)
12. Christensen J, Willatzen M, Velasco VR, Lu MH. 2016 Parity-time synthetic phononic media. *Phys. Rev. Lett.* **116**, 207601. (doi:10.1103/PhysRevLett.116.207601)
13. Liu T, Zhu X, Chen F, Liang S, Zhu J. 2018 Unidirectional wave vector manipulation in two-dimensional space with an all passive acoustic parity-time-symmetric metamaterials crystal. *Phys. Rev. Lett.* **120**, 124502. (doi:10.1103/PhysRevLett.120.124502)

14. Wu Q, Chen Y, Huang G. 2019 Asymmetric scattering of flexural waves in a parity-time symmetric metamaterial beam. *J. Acoust. Soc. Am.* **146**, 850–862. (doi:10.1121/1.5116561)
15. Domínguez-Rocha V, Thevamaran R, Ellis F, Kottos T. 2020 Environmentally induced exceptional points in elastodynamics. *Phys. Rev. Appl.* **13**, 014060. (doi:10.1103/PhysRevApplied.13.014060)
16. Rosa MI, Mazzotti M, Ruzzene M. 2021 Exceptional points and enhanced sensitivity in PT-symmetric continuous elastic media. *J. Mech. Phys. Solids* **149**, 104325. (doi:10.1016/j.jmps.2021.104325)
17. Shmuel G, Moiseyev N. 2020 Linking scalar elastodynamics and non-Hermitian quantum mechanics. *Phys. Rev. Appl.* **13**, 024074. (doi:10.1103/PhysRevApplied.13.024074)
18. Fleury R, Sounas D, Alu A. 2015 An invisible acoustic sensor based on parity-time symmetry. *Nat. Commun.* **6**, 1–7. (doi:10.1038/ncomms6905)
19. Hou Z, Assouar B. 2018 Tunable elastic parity-time symmetric structure based on the shunted piezoelectric materials. *J. Appl. Phys.* **123**, 085101. (doi:10.1063/1.5009129)
20. Heiss W. 1999 Phases of wave functions and level repulsion. *Eur. Phys. J. D* **7**, 1–4. (doi:10.1007/s100530050339)
21. Heiss WD. 2000 Repulsion of resonance states and exceptional points. *Phys. Rev. E* **61**, 929–932. (doi:10.1103/PhysRevE.61.929)
22. Dembowski C, Gräf HD, Harney HL, Heine A, Heiss WD, Rehfeld H, Richter A. 2001 Experimental observation of the topological structure of exceptional points. *Phys. Rev. Lett.* **86**, 787–790. (doi:10.1103/PhysRevLett.86.787)
23. Ding K, Ma G, Xiao M, Zhang ZQ, Chan CT. 2016 Emergence, coalescence, and topological properties of multiple exceptional points and their experimental realization. *Phys. Rev. X* **6**, 021007. (doi:10.1103/PhysRevX.6.021007)
24. Graefe EM, Mailybaev AA, Moiseyev N. 2013 Breakdown of adiabatic transfer of light in waveguides in the presence of absorption. *Phys. Rev. A* **88**, 033842. (doi:10.1103/PhysRevA.88.033842)
25. Uzdin R, Mailybaev A, Moiseyev N. 2011 On the observability and asymmetry of adiabatic state flips generated by exceptional points. *J. Phys. A Math. Theor.* **44**, 435302. (doi:10.1088/1751-8113/44/43/435302)
26. Doppler J *et al.* 2016 Dynamically encircling an exceptional point for asymmetric mode switching. *Nature* **537**, 76–79. (doi:10.1038/nature18605)
27. Xu H, Mason D, Jiang L, Harris J. 2016 Topological energy transfer in an optomechanical system with exceptional points. *Nature* **537**, 80–83. (doi:10.1038/nature18604)
28. Yoon JW *et al.* 2018 Time-asymmetric loop around an exceptional point over the full optical communications band. *Nature* **562**, 86–90. (doi:10.1038/s41586-018-0523-2)
29. Zhang XL, Wang S, Hou B, Chan CT. 2018 Dynamically encircling exceptional points: *in situ* control of encircling loops and the role of the starting point. *Phys. Rev. X* **8**, 021066. (doi:10.1103/PhysRevX.8.021066)
30. Geng L, Zhang W, Zhang X, Zhou X. 2021 Topological mode switching in modulated structures with dynamic encircling of an exceptional point. *Proc. R. Soc. A* **477**, 20200766. (doi:10.1098/rspa.2020.0766)
31. Zhang XL, Jiang T, Chan CT. 2019 Dynamically encircling an exceptional point in anti-parity-time symmetric systems: asymmetric mode switching for symmetry-broken modes. *Light Sci. Appl.* **8**, 88. (doi:10.1038/s41377-019-0200-8)
32. Peng P, Cao W, Shen C, Qu W, Wen J, Jiang L, Xiao Y. 2016 Anti-parity-time symmetry with flying atoms. *Nat. Phys.* **12**, 1139–1145. (doi:10.1038/nphys3842)
33. Yang F, Liu YC, You L. 2017 Anti-PT symmetry in dissipatively coupled optical systems. *Phys. Rev. A* **96**, 053845. (doi:10.1103/PhysRevA.96.053845)
34. Choi Y, Hahn C, Yoon JW, Song SH. 2018 Observation of an anti-PT-symmetric exceptional point and energy-difference conserving dynamics in electrical circuit resonators. *Nat. Commun.* **9**, 2182. (doi:10.1038/s41467-018-04690-y)
35. Fan H, Chen J, Zhao Z, Wen J, Huang YP. 2020 Antiparity-time symmetry in passive nanophotonics. *ACS Photonics* **7**, 3035–3041. (doi:10.1021/acsphotonics.0c01053)
36. Jiang Y, Mei Y, Zuo Y, Zhai Y, Li J, Wen J, Du S. 2019 Anti-parity-time symmetric optical four-wave mixing in cold atoms. *Phys. Rev. Lett.* **123**, 193604. (doi:10.1103/PhysRevLett.123.193604)
37. Wen J, Jiang X, Jiang L, Xiao M. 2018 Parity-time symmetry in optical microcavity systems. *J. Phys. B* **51**, 222001. (doi:10.1088/1361-6455/aae42f)

38. Yang Y, Wang YP, Rao JW, Gui YS, Yao BM, Lu W, Hu CM. 2020 Unconventional singularity in anti-parity-time symmetric cavity magnonics. *Phys. Rev. Lett.* **125**, 147202. (doi:10.1103/PhysRevLett.125.147202)
39. Haken H. 1983 *Synergetics, an introduction*. New York, NY: Springer.
40. Stenholm S. 1984 *Foundations of laser spectroscopy*. New York, NY: Wiley-Interscience.
41. Lugiato L, Prati F, Brambilla M. 2015 *Nonlinear optical systems*. Cambridge, UK: Cambridge University Press.
42. Feng L, El-Ganainy R, Ge L. 2017 Non-Hermitian photonics based on parity-time symmetry. *Nat. Photonics* **11**, 752–762. (doi:10.1038/s41566-017-0031-1)
43. Li H, Mekawy A, Krasnok A, Alù A. 2020 Virtual parity-time symmetry. *Phys. Rev. Lett.* **124**, 193901. (doi:10.1103/PhysRevLett.124.193901)
44. Huang J, Zhou X. 2020 Non-reciprocal metamaterials with simultaneously time-varying stiffness and mass. *J. Appl. Mech.* **87**, 071003. (doi:10.1115/1.4046844)
45. Ashida Y, Gong Z, Ueda M. 2020 Non-Hermitian physics. *Adv. Phys.* **69**, 249–435. (doi:10.1080/00018732.2021.1876991)
46. Milburn TJ, Doppler J, Holmes CA, Portolan S, Rotter S, Rabl P. 2015 General description of quasiadiabatic dynamical phenomena near exceptional points. *Phys. Rev. A* **92**, 052124. (doi:10.1103/PhysRevA.92.052124)
47. Gilary I, Mailybaev AA, Moiseyev N. 2013 Time-asymmetric quantum-state-exchange mechanism. *Phys. Rev. A* **88**, 010102. (doi:10.1103/PhysRevA.88.010102)
48. Diener M. 1984 The canard unchained *or* how fast/slow dynamical systems bifurcate. *Math. Intell.* **6**, 38–49. (doi:10.1007/BF03024127)